Generation of photonic tensor network states with Circuit QED

Zhi-Yuan Wei,[1,2,*] J. Ignacio Cirac,[1,2] and Daniel Malz[1,2,†]

[1] *Max-Planck-Institut für Quantenoptik, Hans-Kopfermann-Straße 1, D-85748 Garching, Germany*
[2] *Munich Center for Quantum Science and Technology (MCQST), Schellingstr. 4, D-80799 München, Germany*

(Dated: September 15, 2021)

We propose a circuit QED platform and protocol to deterministically generate microwave photonic tensor network states. We first show that using a microwave cavity as ancilla and a transmon qubit as emitter is a favorable platform to produce photonic matrix-product states. The ancilla cavity combines a large controllable Hilbert space with a long coherence time, which we predict translates into a high number of entangled photons and states with a high bond dimension. Going beyond this paradigm, we then consider a natural generalization of this platform, in which several cavity–qubit pairs are coupled to form a chain. The photonic states thus produced feature a two-dimensional entanglement structure and are readily interpreted as *radial plaquette* projected entangled pair states [1], which include many paradigmatic states, such as the broad class of isometric tensor network states, graph states, string-net states.

I. INTRODUCTION

Producing large-scale entangled photonic states is central to many quantum technologies, including computing [2], cryptography [3], networks [4], or sensing [5]. The standard method for producing multi-photon entanglement utilizes parametric down-conversion (PDC) [6], which has been used to produce 12-photon entanglement [7]. However, this method possesses certain limitations, notably the exponential decrease of success probability with photon number. One promising way to overcome that is to deterministically and sequentially generate a string of entangled photons using a single quantum emitter [8–14]. The class of states that can be sequentially generated coincides with the set of matrix product states (MPS) [10], a type of tensor network states (TNS) that widely appears in one-dimensional quantum many-body systems [15–18]. Some of the sequential photon generation protocols have been experimentally realized in quantum dots [19] and circuit QED [20, 21]. Using coupled emitters [22–26] or allowing the emitted photons to travel back and interact with the photon source again [27–33], it is possible to produce TNS with a higher-dimensional entanglement structure.

It has recently been shown that all higher-dimensional photonic states thus produced belong to the class of *radial plaquette* projected entangled pair states (rp-PEPS) [1], a general class obtained through the sequential application of geometrically local unitaries in the form of plaquettes of side length L_p. rp-PEPS contain isometric tensor network states (isoTNS) as a subclass [34], which are PEPS [15–18] subject to an isometry condition. This immediately implies that rp-PEPS include important states like the graph states with local connectivities [24, 35], toric code states [36, 37], all string-net states [38–41] [42] and hypergraph states with local connectivities [43]. The experimental preparation of such states in two dimensions is pursued intensely [44–46].

To date, existing platforms and proposals have almost exclusively explored photonic TNS of bond dimension $D = 2$ [8, 9, 12, 13, 19, 21], with one theoretical protocol forming an exception, which is capable of deterministically producing MPS with higher bond dimension using an ordered array of Rydberg atoms [14]. This platform however does not easily extend to produce higher-dimensional TNS. The existing proposals that produce higher-dimensional TNS are also mostly limited to $D = 2$, and particularly focus on the cluster state generation. One notable exception is the protocol in Ref. [28], which probabilistically produces two-dimensional TNS with $D > 2$ utilizing the PDC process in an optical loop. Thus, despite significant efforts, there are still important theoretical challenges on how to deterministically produce high-fidelity and high-bond-dimension photonic TNS in one and particularly in higher dimensions.

In this work, we propose a circuit QED platform capable of deterministically generating (microwave) photonic rp-PEPS with the so-called *source point* [1] in one corner of the lattice. We consider a cavity dispersively coupled to a transmon qubit and show that this allows one to generate MPS of moderately high bond dimension and a large number of entangled photons, which is outstanding among currently available platforms. Using current experimental parameters, our simulations indicate that this platform has the potential to deterministically generate a one-dimensional cluster state of with a large number of photons using current technologies, which would improve the experimental results in Ref. [21] severalfold. We then show that using an array of m such MPS sources one can efficiently generate rp-PEPS. The circuit depth in terms of plaquette unitaries to prepare such a state on a $n \times m$ lattice of photons asymptotically scales as [1]

$$\mathcal{T} \approx L_p \cdot n + m. \tag{1}$$

Since rp-PEPS is a large class, our platform allows one

* zhiyuan.wei@mpq.mpg.de
† daniel.malz@mpq.mpg.de

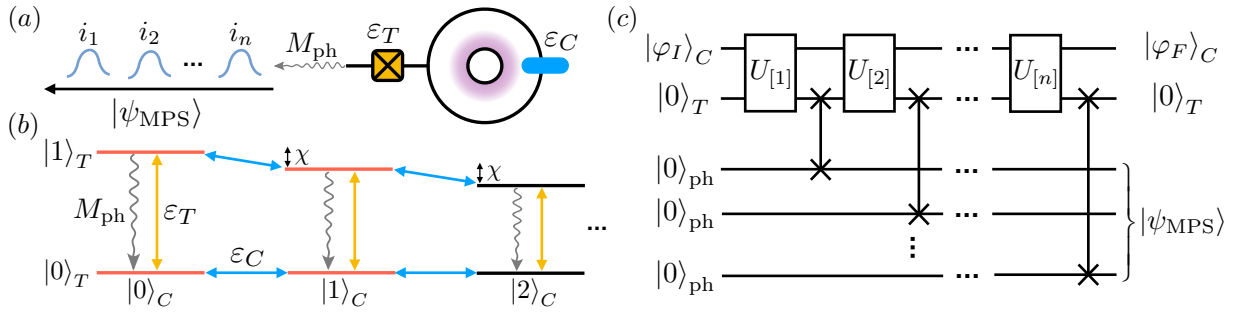

FIG. 1. Generating photonic matrix product states (MPS) with circuit QED. (a) We consider a cavity dispersively coupled to a transmon, which can be controlled by driving both the cavity (ε_C) and the transmon (ε_T). The transmon excitation can be converted into a traveling microwave photon. By sequentially applying unitary operations followed by photon emissions $M_{\rm ph}$, one can produce a chain of entangled photons. (b) The level diagram of the system. The levels in red are used in the protocol for $D = 2$ MPS generation. The yellow (blue) arrows correspond to driving the transmon (cavity). (c) Quantum circuit of the MPS generation protocol. Photon emission ($M_{\rm ph}$) is represented by a SWAP gate.

to create photonic states useful for applications in quantum computing [35, 43], metrology [47–49], communication and networking [50], and that exhibit topological order [36, 37, 40, 41].

The rest of the article is structured as follows. In section II, we present our setup to generate arbitrary MPS using a microwave cavity coupled to a transmon qubit, discuss the imperfections during the MPS generation, and estimate the performance of the device. In section III, we present the setup to generate photonic rp-PEPS and provide the circuits for generating the two-dimensional cluster state, the toric code state, and isoTNS. At last, we analyze the scaling of the state preparation fidelity. We summarize our work in section IV.

II. GENERATING MPS WITH CQED

In this section, first we introduce the setup in section II A and the MPS generation protocol in section II B. Then we analyze the imperfections during the protocol in section II C, and shown in section II D that this protocol can be implemented with current technologies with potentially outstanding performance.

A. cQED sequential photon source

We consider the setup sketched in Fig. 1(a), where a cavity (with the Hilbert space $\mathcal{H}_C$) is dispersively coupled to a transmon qubit (with the Hilbert space $\mathcal{H}_T$), with a Hilbert space $\mathcal{H}_{\rm src} = \mathcal{H}_T \otimes \mathcal{H}_C$ [51]. The transmon ground (excited) state is denoted by $|0\rangle_T$ ($|1\rangle_T$). Defining the transition operator $\sigma_{\alpha\beta} = |\alpha\rangle_T \langle\beta|$ for the transmon, the system Hamiltonian $H_{\rm src}(t) = H_0 + H_{\rm drive}(t)$ contains a static part

$$H_0 = \omega_T \sigma_{11} + \omega_C a^\dagger a - \chi \sigma_{11} a^\dagger a, \tag{2}$$

and time-dependent driving of transmon and cavity

$$H_{\rm drive}\,(t) = \varepsilon_C(t) a + \varepsilon_T(t) \sigma_{01} + \text{ H.c.} \tag{3}$$

Here ω_T (ω_C) is the frequency of the transmon qubit (cavity), and a is the lowering operator of the cavity mode. The dispersive interaction strength χ sets a timescale for cavity-transmon gates. The driving amplitude of the qubit (cavity) is ε_T (ε_C). The level structure of this system is shown in Fig. 1(b). This Hamiltonian gives universal control of the cavity-transmon system [52]. We assume that one can engineer the following on-demand photon emission process $M_{\rm ph}$ from the transmon excitation

$$M_{\rm ph}: \quad |i\rangle_T \to |0\rangle_T |i\rangle_{\rm ph}, \quad i = 0, 1. \tag{4}$$

This can for example be achieved by coupling the qubit to an additional emitter via a tunable coupler [21].

B. MPS generation protocol

The setup in section II A can sequentially generate photonic matrix product states (MPS) using the generic protocol proposed in Ref. [10], schematically shown in Fig. 1(c). We identify the first D Fock states of the cavity mode as our basis for the D-level ancilla, with a Hilbert space $\mathcal{H}_\mathcal{D}$. The MPS generation protocol starts from an ancilla initial state $|\varphi_I\rangle_C \in \mathcal{H}_D$ with the transmon in its ground state. In each photon generation round, the ancilla first interacts with the transmon, described by a unitary operation $U_{[i]}$. Then, the transmon emits its excitation and returns to its ground state (denoted by a SWAP gate in Fig. 1c), generating a photonic qubit defined by the presence or absence of a photon at that time. This setup is notably different from Ref. [11], where a D-level atom is used as the ancilla, and an optical cavity is used to emit photons.

In the whole protocol, the unitaries always act on the ancilla-transmon states of form $|\varphi\rangle_C|0\rangle_T$, that is

$$U_{[i]}\left(|\varphi\rangle_C|0\rangle_T\right)=\sum_{j=0}^{1}V_{[i]}^{j}|\varphi\rangle_C|j\rangle_T. \tag{5}$$

Since $U_{[i]}$ is unitary, the matrices $\{V_{[i]}^{j}\}$ satisfy the isometry condition $\sum_{j=0}^{1}V_{[i]}^{j\dagger}V_{[i]}^{j}=I_D$. The quantum state after n rounds of photon generation is $|\Psi\rangle=M_{\rm ph}U_{[n]}\dots M_{\rm ph}U_{[1]}\,|\varphi_I\rangle_C$. By disentangling the ancilla and the photonic states in the last step such that $|\Psi\rangle=|\varphi_F\rangle_C\otimes|\psi_{\rm MPS}\rangle$, one generates the following photonic MPS [10]

$$|\psi_{\rm MPS}\rangle\propto\sum_{i_1\dots i_n=0}^{1}{}_C\langle\varphi_F|V_{[n]}^{i_n}\dots V_{[1]}^{i_1}|\varphi_I\rangle_C\,|i_n\dots i_1\rangle\,. \tag{6}$$

We use the quantum optimal control (QOC) approach developed in Ref. [14] (which is based on Ref. [53]) to find the pulse sequences that implement the desired unitary operations for our protocol (see details in Appendix A). As a demonstration, we show how to generate a linear cluster state [54] that can be written as an MPS of bond dimension $D=2$, with

$$\begin{aligned}&V_{[i]}^{0}=\tfrac{1}{\sqrt{2}}\begin{pmatrix}1&0\\1&0\end{pmatrix},\quad V_{[i]}^{1}=\tfrac{1}{\sqrt{2}}\begin{pmatrix}0&1\\0&-1\end{pmatrix},\\&|\varphi_I\rangle_C=\tfrac{1}{\sqrt{2}}(|0\rangle+|1\rangle),\quad |\varphi_F\rangle_C=|0\rangle.\end{aligned} \tag{7}$$

In each round except the last, we apply the same unitary $U_{[i\neq n]}$ followed by photon emission represented by $M_{\rm ph}$, which adds one site to the state. In the last step, we apply the unitary $U_{[n]}$ followed by $M_{\rm ph}$, which emits the last photon and disentangles the source from the photons. The pulse sequence of the driving [Eq. (3)] for implementing the two unitaries is shown in Fig. 2, and more details are provided in Appendix A.

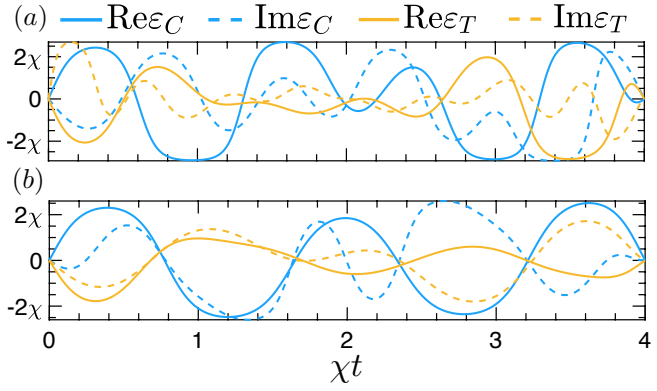

FIG. 2. Optimized pulse of the cavity and transmon driving [Eq. (3)] to implement the unitaries (a) $U_{[i\neq n]}$ and (b) $U_{[n]}$ for the cluster state [Eq. (7)] generation.

C. Analysis of experimental imperfections

Ideally, the above protocol generates the desired pure photonic state $|\psi_{\rm MPS}\rangle$. However, there are various imperfections in this system during the unitary operation and the photon emission process. Thus the protocol produces a n-photon density matrix $\rho_{\rm ph}$, with a non-unit fidelity $\mathcal{F}_{\rm MPS}={}_{\rm ph}\langle\psi_{\rm MPS}|\rho_{\rm ph}|\psi_{\rm MPS}\rangle_{\rm ph}$. Due to the sequential nature of the protocol, $\mathcal{F}_{\rm MPS}$ is an exponentially decaying function of the emitted photon number n, that is

$$\mathcal{F}_{\rm MPS}=e^{-\xi\cdot n}, \tag{8}$$

where ξ is the error per photon emission. An example of this behavior is shown in Fig. 3(a).

Decoherence processes in the cavity-transmon system include transmon decay at a rate Γ_T, cavity mode decay at a rate Γ_C, and transmon dephasing at a rate Γ_ϕ [55]. These processes happen both during the unitary operations and the photon emission process. The finite anharmonicity α of the transmon further allows leakage into the second excited state $|2\rangle_T$ in every unitary operation.

To model the imperfections due to finite anharmonicity α during unitary operations, we model the transmon as a truncated anharmonic oscillator with basis $\{|0\rangle_T,|1\rangle_T,|2\rangle_T\}$. After further including the decoherence effects, the system density matrix $\rho_{\rm src}\in\mathcal{H}_{\rm src}$ evolves under the master equation

$$\begin{aligned}\dot{\rho}_{\rm src}(t)=&\,i[H'_{\rm src}(t),\rho_{\rm src}(t)]\\&+\sum_n\left(J_n\rho_{\rm src}(t)J_n^\dagger-\frac{1}{2}\{\rho_{\rm src}(t),J_n^\dagger J_n\}\right),\end{aligned} \tag{9}$$

with $H'_{\rm src}(t)$ being the system Hamiltonian including transmon double excitations with anharmonicity α. Defining the spin operators $\sigma_{ij}=|i\rangle_T\langle j|$, the jump operators are $J_T=\sqrt{\Gamma_T}(\sigma_{01}+\sqrt{2}\sigma_{12}),J_C=\sqrt{\Gamma_C}a$, $J_\phi=\sqrt{\Gamma_\phi}(\sigma_{11}+2\sigma_{22})$.

Since the current experiments generally have $|\alpha|\gg|\chi|\gg\Gamma_C,\Gamma_T,\Gamma_\phi$ [51, 55, 56], for a gate time $T\sim1/|\chi|$ we can estimate the scale of the errors on $\mathcal{F}_{\rm MPS}$ during each unitary operation perturbatively. The total error ξ is a sum of several parts: (i) transmon decay ξ_{Γ_T}, (ii) transmon dephasing ξ_{Γ_ϕ}, (iii) cavity decay ξ_{Γ_C}, and (iv) transmon nonlinearity ξ_α. These contributions scale as

$$\begin{aligned}&\xi_{\Gamma_T}\sim\Gamma_T/|\chi|,\qquad &&\xi_{\Gamma_\phi}\sim\Gamma_\phi/|\chi|,\\&\xi_{\Gamma_C}\sim\Gamma_C/|\chi|,\qquad &&\xi_\alpha\sim|\chi|^2/|\alpha|^2.\end{aligned} \tag{10}$$

Imperfections also affect the photon emission process. First, there is a finite intrinsic photon retrieval efficiency $p_{\rm em}$ associated to $M_{\rm ph}$. Second, system decoherence happens during the photon emission. We assume a finite photon emission rate $\Gamma_{\rm em}$, and thus a finite duration of photon emission $T_{\rm em}$ (which we can tune). In the regime of $\Gamma_T,\Gamma_\phi,\Gamma_C\ll\Gamma_{\rm em}$, we can estimate scaling of error on $\mathcal{F}_{\rm MPS}$ due to system decoherences during each emission

process as

$$\begin{aligned} \xi^{\rm em}_{\Gamma_C} &\sim \Gamma_C T_{\rm em}, \qquad \xi^{\rm em}_{\Gamma_T} \sim \Gamma_T/\Gamma_{\rm em}, \\ \xi^{\rm em}_{\Gamma_\phi} &\sim \Gamma_\phi/\Gamma_{\rm em}, \qquad \xi_{p_{\rm em}} \sim -\log p_{\rm em}. \end{aligned} \tag{11}$$

Notably, here $\xi^{\rm em}_{\Gamma_T}$ and $\xi^{\rm em}_{\Gamma_\phi}$, which are due to transmon decoherence, do not depend on the emission time $T_{\rm em}$, since the transmon excitation is emitted out during each emission process. The expression for $\xi_{p_{\rm em}}$ comes from the fact that $e^{-\xi_{p_{\rm em}} n_{\rm ph}} \sim p_{\rm em}^{n_{\rm ph}}$. The finite photon emission time also results in a residual population of the transmon first excited state $p_{T1}(T_{\rm em}) = e^{-\Gamma_{\rm em} T_{\rm em}} \cdot p_{T1}(0)$, which reduces the photon retrieval efficiency $p_{\rm em}$. The whole photon emission process including all imperfections can be described by a process map $W_{\rm ph} : \mathcal{H}_{\rm src} \to \mathcal{H}_{\rm src} \otimes \mathcal{H}_{\rm ph}$ that maps $\rho_{\rm src}$ to a system-photon joint density matrix (see the construction of $W_{\rm ph}$ in Appendix C). At last, note that we did not include the imperfections during photon transmission, which is not a part of our setup.

Using the solution of Eq. (9) and the process map $W_{\rm ph}$, we can use a matrix product density operator (MPDO) approach [14] to obtain the photonic state fidelity $\mathcal{F}_{\rm MPS}$ and extract the overall error rate ξ (details in Appendix B). As a demonstration, we analyze the process of generating the one-dimensional cluster state using the pulses in Fig. 2. From the scaling data of ξ as a function of various imperfections (details in Appendix D), in the regime of small error ($\xi \ll 1$), we have

$$\xi \approx \xi_{\rm unit} + \xi^{\rm src}_{\rm em} + \xi^{\rm ph}_{\rm em}, \tag{12}$$

where the imperfections during unitary operation

$$\xi_{\rm unit} = \beta_0 + \frac{\beta_C \Gamma_C + \beta_T \Gamma_T + \beta_\phi \Gamma_\phi}{|\chi|} + \frac{\beta_\alpha \cdot |\chi|^2}{|\alpha|^2}, \tag{13}$$

the cavity-transmon decoherence during the photon emission process

$$\xi^{\rm src}_{\rm em} = \beta_{\phi,{\rm em}} \Gamma_\phi/\Gamma_{\rm em} + \beta_{C,{\rm em}} \Gamma_C T_{\rm em}, \tag{14}$$

and the imperfections of the photon emission

$$\xi^{\rm ph}_{\rm em} = -\beta_{\rm em} \log\left((1 - e^{-\Gamma_{\rm em} T_{\rm em}}) \frac{\Gamma_{\rm em}}{\Gamma_{\rm em} + \Gamma_T} p_{\rm em} \right). \tag{15}$$

The above overall scaling matches our qualitative prediction [Eqs. (10) and (11)] very well. The non-universal coefficients $\{\beta_i\}$ depend on the target photonic state and the pulse shape, and are extracted from scaling data shown in Appendix C. In our example of cluster state generation, using the pulses shown in Fig. 2, we obtain

$$\begin{aligned} &\beta_C = 2.20, \quad \beta_T = 1.43, \quad \beta_\phi = 0.92, \\ &\beta_{\phi,{\rm em}} = 0.51, \quad \beta_{C,{\rm em}} = 0.47, \quad \beta_{\rm em} = 0.47, \\ &\beta_0 = 2.58 \times 10^{-4}, \quad \beta_\alpha = 46.7. \end{aligned} \tag{16}$$

Here β_0 corresponds to the imperfect synthesis of the optimal control pulse, and can typically be made negligible. All other $\{\beta_i\}$ are of order $O(1)$, except β_α which correspond to the effect of transmon double excitations, which is particularly large because it scales with the maximum driving amplitude of the transmon, which can be several times larger than $|\chi|$ [c.f. Fig. 2]. Note that, the decoherence due to transmon double excitations [c.f. Eq. (13)] is still relatively small, thanks to the strong anharmonicity $|\alpha|$ that suppress the transmon double excitations.

D. Performance estimation of protocol

We estimate the performance of this sequential photon source with current state-of-the-art experimental parameters. Specifically, the cavity and transmon parameters are $\Gamma_C = 0.37\,{\rm kHz}$, $\Gamma_T = 5.88\,{\rm kHz}$, $\Gamma_\phi = 23.26\,{\rm kHz}$, $\alpha = 2\pi \times -236\,{\rm MHz}$, $\chi = 2\pi \times -2.194\,{\rm MHz}$ [55], and the photon emission parameters are $\Gamma_{\rm em} = 2\pi \times 1.95\,{\rm MHz}$, $p_{\rm em} = 1$ [21]. We also choose an optimal duration of photon emission as $T^{\rm opt}_{\rm em} = \log(1 + \beta_{\rm em}\Gamma_{\rm em}/\beta_{\rm C,em}\Gamma_C)/\Gamma_{\rm em}$ to minimize ξ [c.f. Eq. (12)], under the assumption of a fixed photon emission rate $\Gamma_{\rm em}$. For the one-dimensional cluster state generated using the pulse sequence in Fig. 2, the MPDO evolution of the fidelity $\mathcal{F}_{\rm MPS}$ with this set of parameters is shown in Fig. 3(a). Defining the *entanglement length* $N_{\rm ph} = \log 2/\xi$ (recall ξ defined in Eq. (8)), which is the photon number that the fidelity drops down to $\mathcal{F}_{\rm MPS} = 1/2$. For Fig. 3(a) we obtain $N_{\rm ph} \approx 123$, which would mean over an eightfold increase compared to the experimentally demonstrated $N_{\rm ph} \approx 15$ in Ref. [21]. This improvement partly comes from the fact that we exploit the long transmon lifetime reported in Ref. [55]. If we use the transmon properties reported in [21], our protocol gives $N_{\rm ph} \approx 47$ (see Appendix D), which is still a substantial improvement.

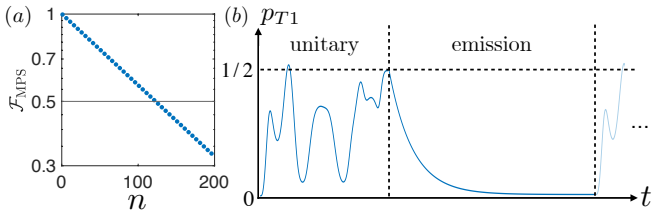

FIG. 3. (a) The state fidelity versus the number of photons for the cluster state generated using the pulse sequence in Fig. 2, with the state-of-the-art parameters listed in section II D. The horizontal line denotes $\mathcal{F}_{\rm MPS} = 1/2$, with the corresponding photon number $N_{\rm ph}$ defined as the *entanglement length* of the photon string. (b) Evolution of the transmon excited population p_{T1} during one sequence of cluster state generation. The p_{T1} shows a transient evolution during the unitary operation driven by the pulse in Fig. 2(a), and exponentially decays during the photon emission process.

To illustrate this point, we plot the population p_{T1} of the transmon excited state $|1\rangle_T$ during one photon generation round in Fig. 3(b). We see that $|1\rangle_T$ is only transiently populated during the unitary operation (driven by the pulse in Fig. 2a), compared to the protocol in Ref. [21] where one always has $p_{T1} = 1/2$ during the cluster state

generation. This leads to a substantial improvement of the entanglement length obtained in our protocol.

At last, we estimate the scaling of $N_{\rm ph}$ with the bond dimension D of the desired MPS as (see Appendix D 3)

$$N_{\rm ph} \propto D^{-2}, \tag{17}$$

and this scaling mainly comes from the time $T^D_{\rm MPS} = O(D^2)$ [57] to implement each unitary that acts on the system of dimension $\dim \mathcal{H}_{\rm src} = 2D$ [c.f. section II B]. This scaling indicates that our system can create MPS of moderately high bond dimensions. This already finds many applications and can capture the ground states of one-dimensional local gapped Hamiltonians [58–61]. Even for one-dimensional spin models at a critical point, a moderately high D is suitable to capture the ground state of the chain with moderate system size, as the main deviation to the thermodynamic limit comes from the finite size effect, instead of a finite-entanglement effect due to the limited D [62].

III. GENERATING RP-PEPS WITH CQED

The previous section shows that this cavity-transmon system has the capacity to produce high-fidelity one-dimensional photonic MPS. In this section, we demonstrate how to extend the cavity-transmon system to implement the high-dimensional photonic state generation protocol introduced in Ref. [1]. First, in section III A we introduce the array of coupled sequential photon sources and prove the universality of the Hamiltonian for this system, which allows this system to implement arbitrary local unitary transformations. Then we show in section III B that, using this setup, one can generate radial plaquette PEPS (rp-PEPS), whose *source point* [c.f. section III B] sits on a corner of the lattice. After that, in section III C we demonstrate this protocol by discussing the preparation of two-dimensional cluster state, the toric code state, and the isometric tensor network states (isoTNS). At last, we analyze the scaling of the state preparation fidelity for this protocol in section III D. Here we mainly focus on generating two-dimensional photonic states, however, this protocol readily extends to higher dimensions [1].

A. Setup: array of sequential photon sources

Let us consider a natural generalization of the setup in section II A, which we have a quasi-one-dimensional array consisting of $L_c \times m$ cavity-transmon pairs, and use each D' Fock states of each cavity. Here we use the L_c cavities in each row to form an ancilla A of dimension $D = D'^{L_c}$, which will be needed for the photon generation protocol in section III B. Both the L_c and D' can be chosen at will, and we will comment on the choice of them in section III D. Moreover, among all $L_c \times m$ transmons, there are m transmon *emitters* $\{T_j\}_{j=1,\dots,m}$ (one in each row, see Fig. 4a) that can emit photons, while other transmons are used to provide universal control to the corresponding cavities [63].

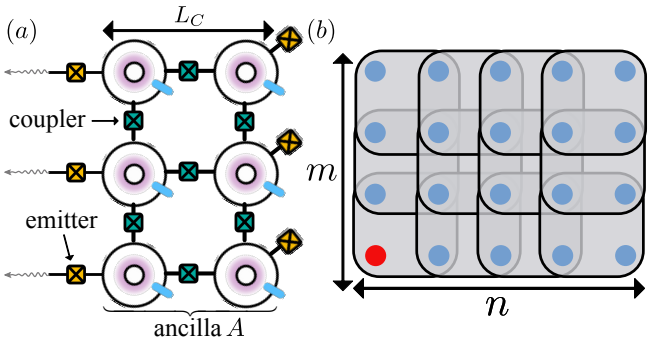

FIG. 4. (a) The setup to generate photonic radial plaquette PEPS (rp-PEPS), which consist a quasi-one-dimensional array of cavity-transmon pairs (the notations follow that in Fig. 1a). In each row there is a transmon emitter that can emit photons. The neighboring cavities are connected by Y-shape couplers (the green boxes). (b) rp-PEPS with open boundary conditions are produced by sequential applying unitaries on overlapping regions. Here the *source point* [1] of the state is denoted by the red dot.

We couple each neighboring pair of cQED sequential photon sources by a coupler that interacts with both cavities [64] (shown as green boxes in Fig. 4a). By driving the coupler with two-tone pumps, the four-wave mixing process of the coupler reduces to the following bilinear interaction [65]

$$H^{ij}_{\rm int}(t) = g_{ij}(t)(e^{i\varphi_{ij}(t)}a^\dagger_i a_j + \text{H.c.}). \tag{18}$$

Here $a^\dagger_i$ denote the creation operator of the cavity for i-th cQED sequential photon source. The coupling strength $g_{ij}(t)$ and phase $\varphi_{ij}(t)$ can be controlled by the drivings of the coupler. Let us denote the set of vertices of the square lattice of sources in Fig. 4(a) as $\mathcal{V}$, where each vertex v_{ij} connects the cavities of the i-th and j-th source. One can thus write down the Hamiltonian of this system as

$$H_{\rm array}(t) = \sum_{i=1}^{L_c\times m} H^i_{\rm src}(t) + \sum_{v_{ij}\in\mathcal{V}} H^{ij}_{\rm int}(t), \tag{19}$$

where $H^i_{\rm src}$ is the Hamiltonian for the i-th cQED sequential photon source, containing the terms in Eqs. (2) and (3). Equipped with the universal control of each cQED sequential photon source and the bilinear couplings, we prove in Appendix F that $H_{\rm array}$ can universally control the whole array of cQED sequential photon sources. Given this, we can assume that one can implement arbitrary local unitary operations one this system.

In sum, this system can be represented by a one-dimensional array of D'^{L_C}-level ancillas (labeled by $\{A_j\}_{j=1,\dots,m}$) coupled to transmon emitters (labeled by $\{T_j\}_{j=1,\dots,m}$), illustrated in Fig. 5. Note that one can let

more transmons in each row to emit photons, which effectively increase the dimension of the transmon emitters. At last, in the next sections we will treat each ancilla effectively as $L_p - 1$ qubits by choosing D' and L_c such that $D'^{L_C} \geq 2^{L_p-1}$.

B. Preparation of rp-PEPS

Ref. [1] introduces a generic protocol to produce rp-PEPS on flying qubits. rp-PEPS are states prepared by sequentially applying unitaries on plaquettes of size $L_p \times L_p$ ($L_p \ll n, m$) in a radial fashion, where one example is illustrated in Fig. 4(b). They possess long-range correlations and area-law entanglement, and photonic rp-PEPS can be efficiently prepared with the circuit depth Eq. (1).

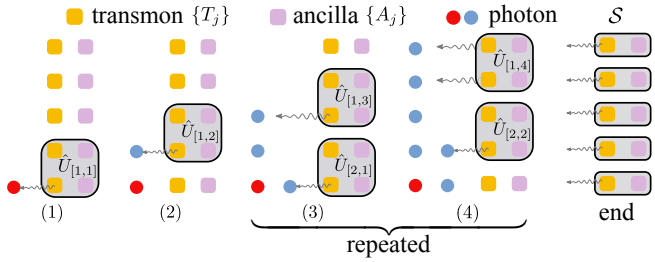

FIG. 5. The preparation of photonic rp-PEPS. In the preparation of the (i, j)-th site, we apply a unitary $\hat{U}_{[i,j]}$ followed by a photon emission of the transmon T_j. After the initial steps (1) and (2), steps (3) and (4) will be repeated. At the end of the protocol, we swap the excitations on the ancillas to the emitters and then convert them to photons, denoted as $\mathcal{S}$.

The generation procedure of rp-PEPS is shown in Fig. 5. We start from an initial state where all the ancillas and the transmons are in their ground state $|\varphi_0\rangle = |0_{\{A_j\}}\rangle \otimes |0_{\{T_j\}}\rangle$, and apply unitaries $\{\hat{U}_{[i,j]}\}$ at each step, which acts on ancillas $\{A_j, ..., A_{j+L_p-1}\}$ and transmons $\{T_j, ..., T_{j+L_p-1}\}$. This is equivalent to acting on a plaquette of qubits of size $L_p \times L_p$. After each unitary, we trigger the photon emission from the transmon T_j (denoted as isometry M^j_{ph} [cf. Eq. (4)]). Note that after the last unitary per column, the last emission process per column $M^{m-L_p+1}_{\text{ph}}$ (see step 4 of Fig. 5c) convert excitations of transmons $\{T_{m-L_p+1}, ..., T_m\}$ to multiple photonic qubits at the same time. Repeatedly applying this procedure following the order shown in Fig. 5 (also see the below Eq. (20)), and in the end emitting the remaining excitations in the ancillas (an operation collectively denoted by as $\mathcal{S}$), we generate the desired two-dimensional photonic state [1]

$$|\psi_{\text{rp}}\rangle = \langle\varphi_0|\mathcal{S} \prod_{i=1}^{n-L_p+1} \prod_{j=1}^{m-L_p+1} (M^j_{\text{ph}} \hat{U}_{[i,j]})|\varphi_0\rangle. \quad (20)$$

Given the universal control of Eq. (19), this protocol can produce arbitrary states of form Eq. (20) (schematically shown in Fig. 4b), which are two-dimensional rp-PEPS of plaquette size L_p with open boundary condition, with its *source point* located at the first photon being created [1] [66]. Also note that, in the above protocol, the photon emissions reset the transmons. This allows one to efficiently reuse them, which allows one to parallelize the preparation procedure (shown in steps 3 and 4 of Fig. 5c), such that the circuit depth for preparing rp-PEPS of plaquette length L_p on a $n \times m$ lattice asymptotically scales as Eq. (1) [1]. This system further allows increasing the plaquette size by increasing the number of cavity-transmon pairs L_C and using more modes D' in the cavity.

Finally we note that by replacing the photon emissions with qubit measurements, this state generation protocol naturally becomes a qubit-efficient quantum variational scheme [67, 68].

C. Examples

1. *Two-dimensional cluster state*

Consider a two-dimensional square lattice, with the position vector of each site denoted as $\vec{a} \equiv (i, j)$. The two-dimensional cluster state $|\text{Cl}\rangle_{\text{2D}}$ can be defined in a constructively way, by first preparing all qubits in the state $|+\rangle = \left(|0\rangle + |1\rangle\right)/\sqrt{2}$, denoted as $\bigotimes_{\{\vec{a}\}} |+\rangle$. Then one apply control-Z (CZ) gates between each nearest-neighbouring paris of qubits, which lead to [54]

$$|\text{Cl}\rangle_{\text{2D}} = \prod_{\vec{b} \text{ adjacent } \vec{a}} \text{CZ}_{\vec{a}\vec{b}} \bigotimes_{\{\vec{a}\}} |+\rangle. \quad (21)$$

This state is an rp-PEPS of plaquette size $L_p = 2$, thus it can be prepared by the protocol in section III B, where each ancilla consists of a qubit. The preparation procedure is shown in Fig. 6, where the corresponding plaquette unitaries $\{U_{[i,j]}\}$ in Eq. (20) are formed by CZ, SWAP, and Hadamard gates to create the desired graph state geometry needed for $|\text{Cl}\rangle_{\text{2D}}$.

One can easily extend the size of the state shown along the horizontal direction by repeatedly applying the steps 5.1-8 in Fig. 6, and along the vertical direction by putting more ancilla-transmon pairs and applying unitaries that are similar to step 7. Moreover, by omitting some photon emissions, one can create arbitrary graph states of local connectivities in this way [24].

The depth for this circuit in terms of plaquette unitaries to prepare $|\text{Cl}\rangle_{\text{2D}}$ of size $n \times m$ is $\mathcal{T} \approx 2n + m$ [c.f. Eq. (1)]. We also point out that this can be further improved to $\mathcal{T}_{\text{cl}} \approx 2n$, since the CZ gates commute with each other. As an example, steps 1-4 in Fig. 6 can be combined such that we parallelly apply CZ gates on all adjacent pairs in the ancilla-transmon array (which can be contained in two layers of plaquette unitaries), then

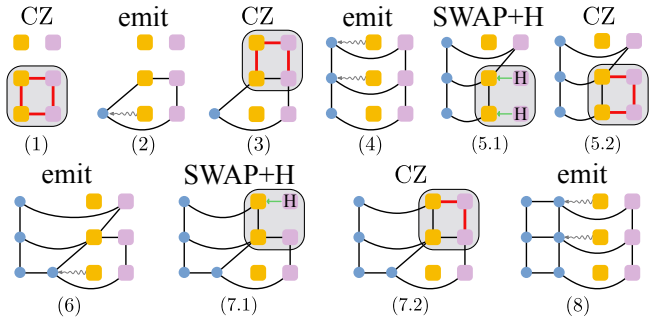

FIG. 6. Preparing two-dimensional cluster state $|\mathrm{Cl}\rangle_{2\mathrm{D}}$ following the rp-PEPS preparation protocol [c.f. Fig. 5, and we keep the same notation as there]. Here both the ancillas and transmons are qubits, and they are initialized in the state $|+\rangle$. The connecting lines between two qubits mean that they have been acted by a control-Z (CZ) gate, with the red color denotes that the CZ gates are being acted in that step. The steps from 1 to 4 prepare the first column of photons. Then in creating the next column of photons, in each unitary we first swap certain ancilla states their corresponding transmons (illustrated by green arrows) and apply Hadamard gates to set the ancilla states to $|+\rangle$ (see 5.1 and 7.1) before applying CZ gates, which eventually prepare the second column (see step 8). By repeating the step 5.1 to 8, we can prepare $|\mathrm{Cl}\rangle_{2\mathrm{D}}$ of arbitrary size.

emit one column of photons. The CZ gates between two cavities can be realized by combining single-qubit rotations and a CNOT gate, which has been experimentally implemented in Ref. [69].

The above further parallization of the circuit show a generic feature of photonic rp-PEPS [Eq. (20)]: in cases where the sequential product of unitaries $\hat{U}^i_{\mathrm{col}} = \prod_{j=1}^{m-L_p+1} \hat{U}_{[i,j]}$ for preparing each column of photons can be parallelized as a circuit of depth $O(1)$, it could be benefitial to directly implement $\hat{U}^i_{\mathrm{col}}$ followed by the photon emission of all transmon emitters $\bigotimes_j M^j_{\mathrm{ph}}$ to prepare the i-th column of the rp-PEPS. This also applies to the below protocol for the generation of the toric-code state.

2. *Toric code state*

The toric code state [70, 71] is a paradigm example of string-net states, and finds important applications for quantum error correction. The toric code Hamiltonian on a square lattice is

$$H_{\mathrm{TC}} = -\sum_s A_s - \sum_p B_p, \tag{22}$$

where $A_s = \prod_{i\in s} Z_i$ is a product of Pauli Z operators that acts on a star of the lattice (a green box in Fig. 7a), and the $B_p = \prod_{j\in p} X_j$ is a product of Pauli X operators that acts on a plaquette of the lattice (a red box in Fig. 7a). For the open boundary condition shown in Fig. 7(a), H_{TC} has a ground state $|\mathrm{TC}\rangle$, which have $+1$ eigenvalue on all $\{A_s\}$ and $\{B_p\}$, that $A_s|\mathrm{TC}\rangle = B_p|\mathrm{TC}\rangle = +1|\mathrm{TC}\rangle$. It can be written as an equal superposition of all plaquette configurations as

$$|\mathrm{TC}\rangle \propto \prod_p (\mathbb{I} + B_p) \bigotimes_{\{\vec{a}\}} |0\rangle\,. \tag{23}$$

The toric code state has recently been prepared on a stationary lattice, with the following procedure [45]:

1. Initialize the whole lattice in the state $\bigotimes_{\{\vec{a}\}} |0\rangle$, where all $\langle A_s\rangle = 1$ and $\langle B_p\rangle = 0$.

2. Choosing a qubit for each plaquette as the representative qubit (an example choice is denoted by purple dots in Fig. 7a), and apply Hadamard gate on it.

3. Within each plaquette, sequentially apply CNOTs with the representative qubit as the control and other qubits as targets, with an ordering such that the representative qubits are not changed until the CNOTs in their plaquette have been applied.

Inspired by this procedure, one can prepare $|\mathrm{TC}\rangle$ as a photonic rp-PEPS of $L_p = 2$ using the protocol in section III B, with each ancilla consisting of a single qubit. To ease the notation, in Fig. 7(b) we group the gates in steps 2-3 of the above procedures that act on each plaquette as $\hat{V}$, and the swap gates used to put the ancilla states to transmons as $\hat{S}_u$ and $\hat{S}_{ud}$.

The preparation circuit is shown in Fig. 7(c), where the plaquette unitaries are alternatively formed by $\hat{V}$ or the identity gate I, and their product with swap gates ($\hat{S}_u$ or $\hat{S}_{ud}$). The $\hat{V}$ implement desired operations for each toric code plaquette region, while the photon emission and swap gates will 'push' the qubits toward. After all operations in Fig. 7(c), one obtains $|\mathrm{TC}\rangle$ of size 4×4 on three columns of photonic qubits and the ancilla qubits, shown in Fig. 7(d). By further repeating the steps from 4-9 in Fig. 7(c) and using more ancilla-transmon pairs, one can generate $|\mathrm{TC}\rangle$ of arbitrary size. We also point out that, one can apply the same procedure as described in the two-dimensional cluster state generation protocol [c.f. section III C 1] to obtain a circuit depth $\mathcal{T}_{\mathrm{TC}} \approx 2n$ in terms of plaquette unitaries for generating $|\mathrm{TC}\rangle$ of size $n\times m$.

The schemes presented here for cluster state generation and toric code state generation are directly derived from their circuit generation on stationary lattices, and we use the coupling between ancilla-transmon pairs to realize coupling between photons along the horizontal direction. This idea generally allows one to obtain photonic state generation circuits by utilizing existing circuits on stationary lattices. For example, one can generate string-net states by extending the protocol in section III C 2, using similar circuits as that in Ref. [72].

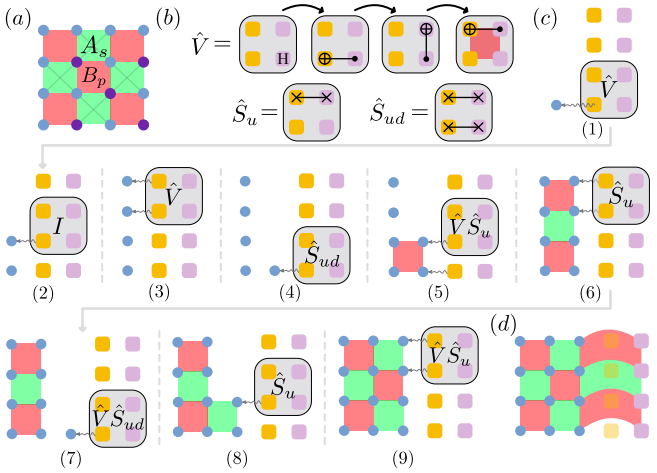

FIG. 7. Preparation of photonic toric code state $|\mathrm{TC}\rangle$ [c.f. Eq. (23)]. Throughout this figure, we keep the same notation as that in Fig. 5. The support of the star operators A_s (plaquette operators B_p) are denoted by the green (red) shades. (a) We consider two-dimensional square lattice of open boundary condition. In this case, $|\mathrm{TC}\rangle$ is the unique ground state of the Hamiltonian H_{TC} [c.f. Eq. (22)], which has $+1$ eigenvalue for all A_s and B_p. Each plaquette has a 'representative qubit', denoted by a purple dot. (b) We group the gates that will be applied to each plaquette as $\hat{V}$. The SWAP gates are denoted as $\hat{S}_u$ and $\hat{S}_{ud}$. (c) The preparation procedure inspired by Ref. [45]. Different steps are separated by dashed grey lines. In each step, we alternatively apply $\hat{V}$ or identity gate I followed by a photon emission (for example, from steps 1 to 3). Also after each photon emission, one needs to swap the corresponding ancilla state to the transmon, thus in steps 4-9 the unitaries are generally the product of swap gates ($\hat{S}_u$ or $\hat{S}_{ud}$) with $\hat{V}$ or I. (d) After step 9 of the panel (c), one obtains $|\mathrm{TC}\rangle$ of size 4×4 with the same geometry as that in panel (a), consisting of three columns of photonic qubits and the column of ancilla qubits. By further repeating the steps from 4-9 in panel (c) and using more ancilla-transmon pairs, one can generate $|\mathrm{TC}\rangle$ of arbitrary size.

3. *Isometric tensor network states*

The rp-PEPS contain the isometric tensor network states [34] (isoTNS) as a subclass [1]. An isoTNS is parametrized by its bond dimension D [34] that bound the entanglement entropy of the state, and its physical dimension d that denote the Hilbert space dimension of each site.

As the protocol in section III B can prepare rp-PEPS with the source point in the corner of the lattice, one can prepare the subclass of isoTNS whose *orthogonality center* (see details in Appendix E) is in this corner. To do so, one has to require the unitaries to have an 'L'-shape [1], as shown in Fig. 8 for the case of $D=2$ and $d=2$. Here each unitary $\hat{B}_{[i,j]}$ acts on the ancilla A_j and transmons $\{T_j,...,T_{j+L_p-1}\}$ to produce isoTNS of bond dimension $D\leq 2^{L_p-1}$. Increasing isoTNS bond dimension corresponds to increasing the arm length of the 'L'-shaped

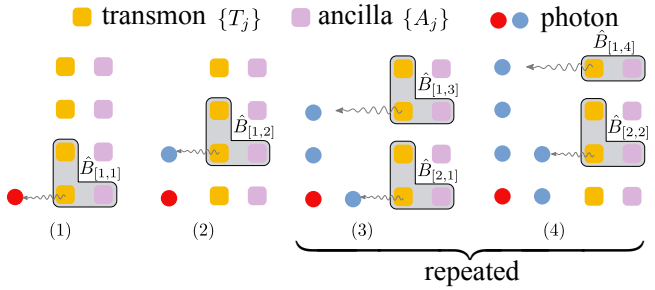

FIG. 8. Preparation of isoTNS with bond dimension $D=2$ and physical dimenison $d=2$. In the preparation of the (i,j)-th site, we apply a unitary $\hat{B}_{[i,j]}$ connecting the cavity C_j and the transmons T_j, T_{j+1}, followed by a photon emission of the transmon T_j. After the initial steps (1 and 2), steps 3 and 4 will be repeated to build up the desired 2D isoTNS. The red dot denotes the orthogonality center of the isoTNS.

unitary. In the end of the protocol, we can disentangle the ancilla from the photonic state being produced [1]. We provide more details on isoTNS in Appendix E.

The subclass of isoTNS whose orthogonality center is in the corner of the lattice already contains all graph states of local connectivities [24] and all string-net states [41], thus the two-dimensional cluster state and toric code state discussed previously can be also created in this way. However, we point out that, the circuits we presented in sections III C 1 and III C 2 are potentially more efficient than the circuit derived from its isoTNS counterpart. For example, the isoTNS representation of arbitrary $\mathbb{Z}_\lambda$ toric code state [73] is shown in Appendix E 1, where the physical dimension of the tensor is λ^4. Thus for the qubit toric code state (the same as that in section III C 2), this isoTNS generation scheme requires each transmon emitter to be 16-dimensional, for which we need to couple multiple transmons to the same ancilla. The existence of isoTNS representation of $\mathbb{Z}_\lambda$ toric code state for arbitrary λ also implies that our scheme can create photonic qudit toric code state, and such states show certain advantages as quantum error-correcting codes compared to the qubit toric code state [74, 75].

At last, isoTNS is a class of state that can be efficiently prepared as shown here (also see Ref. [1]), and serve as an ansatz for classical variational algorithms [34]. Combining these two features may allow one to implement interesting protocols like variational quantum metrology [47–49].

D. Scaling of rp-PEPS generation fidelity

Under imperfections, the rp-PEPS generation protocol [c.f. section III B] will produce a density matrix of photons ρ_{rp}. Here we provide a qualitative estimation of the fidelity $\mathcal{F}_{\mathrm{rp}}=\langle\psi_{\mathrm{rp}}|\rho_{\mathrm{ph}}|\psi_{\mathrm{rp}}\rangle$ of the parallelized version of the rp-PEPS generation protocol. Moreover, one

can calculate the fidelity exactly by extending the MPDO approach in Appendix B.

Let us consider the array shown in Fig. 5(b) with m rows, where each row consists of L_C cavity-transmon pairs, with each cavity and transmon have the decoherence channels that described in section II C. As here we use the first D' Fock states of the cavity, we take the worst-case estimation of the cavity decay rate as $\Gamma'_C = (D'-1)\Gamma_C$.

To prepare a generic rp-PEPS of size $n \times m$ and plaquette length $L_p (L_p \ll n, m)$, when preparing each photon we need to apply a unitary acting on L_p^2 qubits, thus $\dim \hat{U}_{[i,j]} \approx 2^{L_p^2}$. Thus we estimate the time $T_{\rm rp}$ of implementing a generic unitary using optimal control methods as $T_{\rm rp} \sim (\dim \hat{U}_{[i,j]})^2 = O(4^{L_p^2})$ [57]. Since the initial state and the final state of the sources in our protocol are both the ground state $|\varphi_0\rangle$ [c.f. Eq. (20)], in the parallelized preparation procedure [c.f. Fig. 5], each source remain excited for a time $L_p n T_{\rm rp}$. Moreover, there are in total around nm photon emissions. Thus by applying the same argument as in the MPS generation protocol [c.f. section II C], one can estimate the scaling of the fidelity as

$$\mathcal{F}_{\rm rp} \sim \exp\left[-\xi'^{D'}_{\rm unit} \cdot mL_c \cdot L_p n T_{\rm rp} - (\xi'^{{\rm src},D'}_{\rm em} + \xi'^{\rm ph}_{\rm em}) \cdot nm\right], \tag{24}$$

with $\xi'^{D'}_{\rm unit}$, $\xi'^{{\rm src},D'}_{\rm em}$ and $\xi'^{\rm ph}_{\rm em}$ of the same form as that in Eqs. (13) to (15), but with cavity decay rate Γ_C replaced by Γ'_C and different non-universal constants $\{\beta'_i\}$.

Given L_p, the number of cavities in each ancilla L_C is $L_C = \lceil (L_p - 1)/\log_2 D \rceil$. We can thus write overall scaling [Eq. (24)] as $\mathcal{F}_{\rm rp} \sim \exp(-\xi_{\rm rp}^{L_p,D'} \cdot nm)$, with the error rate of generating each photon $\xi_{\rm rp}^{L_p,D'}$ as

$$\xi_{\rm rp}^{L_p,D'} \approx 4^{L_p^2}(L_p - 1)L_p \cdot \xi'^{D'}_{\rm unit}/\log_2 D' + \xi'^{{\rm src},D'}_{\rm em} + \xi'^{\rm ph}_{\rm em}. \tag{25}$$

From the above analysis, we see that using more cavities L_c where each one has a small number of mode D' can reduce the cavity decay rate $\Gamma'_C = (D'-1)\Gamma_C$. However, the fidelity of the inter-cavity connection is generally lower than the single cavity operation [65]. So depending on the desired plaquette length L_p of the rp-PEPS, one needs to choose appropriate L_c and D' to get the highest possible fidelity.

IV. CONCLUSION

In conclusion, we propose a physical platform and a protocol to sequentially generate microwave photonic tensor network states with moderately high bond dimensions based on a dispersively coupled cavity-transmon system. The good coherence properties of microwave cavities lead to favorable scaling of the photon number for the MPS, in particular, we show this platform can potentially create a one-dimensional cluster state of over a hundred photons deterministically with current technology. The good connectivity makes this platform a promising candidate for generating a large class of high-dimensional rp-PEPS, and we show how to create a two-dimensional cluster state, the toric code state, and isoTNS as examples. Our work thus serves as systematic guidance for sequential photon generation experiments in cQED platforms, and can naturally be applied to other dispersively coupled qubit-oscillator systems.

Our work can be extended in many ways. First, there are plenty of ideas to further reduce the imperfections during the protocol by applying error-correction techniques [76, 77], applying error-transparent gates or path-independent gates [78] on the bosonic modes, or applying open system optimal control techniques [53, 79, 80]. Second, the ability to generate strongly correlated photonic tensor network states opens the door of developing quantum information processing protocols that go beyond the MPS [47–49]. One can further simultaneously using coupled arrays of emitters and non-Markovian feedback approaches [27–33] to reduce the component overhead of the system and possibly generate a larger class of photonic states.

ACKNOWLEDGMENTS

We thank Yujie Liu and Alejandro González-Tudela for their insightful discussions. We acknowledge funding from ERC Advanced Grant QUENOCOBA under the EU Horizon 2020 program (Grant Agreement No. 742102) and the European Union's Horizon 2020 research and innovation program under Grant No. 899354 (FET Open SuperQuLAN).

Appendix A: MPS generation with cQED using Quantum Optimal Control Approach

In this section, we introduce our quantum optimal control (QOC) approach (similar to that used in [14]) to implement unitaries on this setup.

We aim to find the driving amplitude $\varepsilon_C(t), \varepsilon_T(t)$ for the control $H_{\rm drive}(t)$ [Eq. (3)] that implements the desired unitary operations $U_{[i]}$ [Eq. (5)] in $\mathcal{H}_D \otimes \mathcal{H}_T$.

Given the target MPS to be prepared [Eq. (6)], one can construct a series of isometries $\{\hat{A}_{[i]}\}$ that needs to be implemented on the system [10]. For generating the n-photon cluster state [Eq. (7)], this construction gives two kinds of isometries $\hat{A}_{[i\neq n]}$ and $\hat{A}_{[n]}$, as well as the ancilla initial state $|\varphi_I\rangle_C$ needed in the protocol [c.f. Eq. (6)]:

$$\hat{A}_{[i\neq n]} = \begin{pmatrix} V^0_{[i]} \\ V^1_{[i]} \end{pmatrix} = \frac{1}{\sqrt{2}} \begin{pmatrix} 1 & 0 \\ 1 & 0 \\ 0 & 1 \\ 0 & -1 \end{pmatrix}, \quad \hat{A}_{[n]} = \begin{pmatrix} 1 & 0 \\ 0 & 0 \\ 0 & 1 \\ 0 & 0 \end{pmatrix}, \quad |\varphi_I\rangle_C = \frac{1}{\sqrt{2}}(|0\rangle_C + |1\rangle_C). \tag{A1}$$

Note here that $\hat{A}_{[n]}$ is different from all other $\hat{A}_{[i\neq n]}$, as it contains an additional operation that disentangle the cavity from the photonic MPS, and lead to the final cavity state $|\varphi_F\rangle_C$ in Eq. (7).

We can embed above $\{\hat{A}_{[i]}\}$ into $U_{[i]}$ to realize Eq. (5). In numerical calculations we keep the first $N_C > D$ Fock states in $\mathcal{H}_C$. Thus $\dim \mathcal{H}_C = N_C$ in our numerical calculation. One can then write $U_{[i]}$ as

$$U_{[i]} = \begin{pmatrix} \hat{A}_{[i]} & B_1 \\ O & B_2 \end{pmatrix}, \tag{A2}$$

with its basis vector permuted as

$$\text{Base}(U_{[i]}) \equiv [\text{Base}(\mathcal{H}_D \otimes \mathcal{H}_T), \text{others}]. \tag{A3}$$

The O is a zero matrix, which physically means that $U_{[i]}$ does not cause the population to leak out of $\mathcal{H}_D \otimes \mathcal{H}_T$. The parts B_1 and B_2 are arbitrary, as long as $U_{[i]}$ is a unitary of dimension $2N_C$. One needs two kinds of unitaries $U_{[i\neq n]}$ and $U_{[n]}$ to generate the above cluster state [14] since we get different $\hat{A}_{[i\neq n]}$ and $\hat{A}_{[n]}$ in Eq. (A1). Each application of $U_{[i\neq n]}$ followed by the photon emission adds one site to the cluster state. The last unitary $U_{[n]}$ followed by a photon emission disentangles the source from the photonic MPS.

For the quantum optimal control (QOC) with our cQED platform with Hamiltonian H_{src} [Eqs. (2) and (3)], we go to the rotating frame to remove energy terms of the transmon and the cavity mode in H_{src}, getting

$$H'_{\text{src}}(t) = \chi\sigma_{11}a^\dagger a + [\varepsilon_C(t)a + \varepsilon_T(t)\sigma_{01} + \text{H.c.}], \tag{A4}$$

and readily apply the QOC algorithm in Ref. [14] with the control Hamiltonian $H'_{\text{src}}(t)$ to find the pulse sequences to implement desired $U_{[i]}$. The pulse sequence to implement $U_{[i\neq n]}$ and $U_{[n]}$ for the cluster state generation are shown in Fig. 2, where we choose $N_C = 5$.

Appendix B: The Matrix-Product Density Operator (MPDO) approach to compute state fidelity

In this section we recall the MPDO approach [14] to compute the fidelity $\mathcal{F}_{\text{MPS}}$ of the photonic state. We can rewrite the master equation Eq. (9) in a vectorized form

$$\frac{d\vec{\rho}_{\text{src}}(t)}{dt} = \mathcal{L}(t)\vec{\rho}_{\text{src}}(t), \qquad \vec{\rho}_{\text{src}} = \sum_{a,b=1}^{N_h} \rho_{ab}|a\otimes\bar{b}\rangle, \tag{B1}$$

Here $\mathcal{L}(t)$ is the Liouville operator, $|a\rangle$ is a basis element in $\mathcal{H}_{\text{src}}$ and $|\bar{a}\rangle$ represent its complex conjugate. The solution of Eq. (B1) is

$$\vec{\rho}_{\text{src}}(T) = \mathcal{T}\{e^{\int_0^T \mathcal{L}(t)dt}\}\vec{\rho}_{\text{src}}(0) = W_{\mathcal{L}}\vec{\rho}_{\text{src}}(0). \tag{B2}$$

The photon emission process can be described by a process map

$$W_{\text{ph}} = \sum_{i,j=0}^{1}\sum_{a,b,c,d=1}^{N_h} W^{ij}_{P,abcd}|c,\bar{d},i,\bar{j}\rangle|a,\bar{b}\rangle, \tag{B3}$$

which maps $\vec{\rho}_{\text{src}}$ with vectorized basis $|a,\bar{b}\rangle$ to a system-photon joint density matrix with vectorized basis $|c,\bar{d},i,\bar{j}\rangle = |c,\bar{d}\rangle\otimes|i,\bar{j}\rangle_{\text{ph}}$. Thus each photon generation round results in a map from the joint density matrix $\vec{\rho}_{[k-1]}$ of $k-1$ photons and system to the joint density matrix $\vec{\rho}_{[k]}$ of k photons and system:

$$\vec{\rho}_{[k]} = \sum_{i_k,j_k=0}^{d-1} N^{i_k,j_k}_{[k]}\vec{\rho}_{[k-1]}, \qquad \text{with} \quad N^{i_k,j_k}_{[k]} = W^{i_kj_k}_{\text{ph}}W_{\mathcal{L}_{[k]}}. \tag{B4}$$

The fidelity $\mathcal{F}_{\text{MPS}}$ can be efficiently evaluated as [14]

$$\mathcal{F}_{\text{MPS}} = \sum_{\{i_k,j_k\}=0}^{1} \text{Tr}[N^{i_n,j_n}_{[n]}...N^{i_1,j_1}_{[1]}\tilde{B}] \times \text{Tr}[(A^{j_n}_{[n]}\otimes\bar{A}^{i_n}_{[n]})...(A^{j_1}_{[1]}\otimes\bar{A}^{i_1}_{[1]})(B\otimes B)], \tag{B5}$$

where we denote $\tilde{B} \equiv \sum_{\alpha=1}^{N_h} |\varphi'_I\rangle\langle\alpha|\otimes|\varphi'_I\rangle\langle\alpha|$, $B \equiv |\varphi_I\rangle\langle\varphi_F|$, and $\bar{A}$ as the complex conjugate of a matrix A. For higher-dimensional rp-PEPS, the $\mathcal{F}_{\text{rp}}$ can be computed in the same way by viewing the high-dimensional rp-PEPS as an MPS with bond dimension and physical dimension scale exponentially with the number of sequential photon sources m.

Appendix C: Construction of process map $W_{\rm ph}$

The decoherence effects and the finite photon retrieval efficiency $p_{\rm em}$ during the photon emission will modify $W_{\rm ph}$ from its ideal form $W_{\rm ph} = M_{\rm ph} \otimes \bar{M}_{\rm ph}$ with $M_{\rm ph}$ of the form Eq. (4). A good way to construct $W_{\rm ph}$ is to include environmental photon modes which capture the erroneous jump events. When there is a finite photon retrieval efficiency $p_{\rm em}$, we can include an environmental photon mode ε_T, and the $M_{\rm ph} : \mathcal{H}_T \to \mathcal{H}_T \otimes \mathcal{H}_{\rm ph} \otimes \mathcal{H}_{\varepsilon_T}$ becomes

$$M_{\rm ph}: \begin{array}{l} |1\rangle_T \to |0\rangle_T(\sqrt{p_{\rm em}}|1\rangle_{\rm ph}|0\rangle_{\varepsilon_T} + \sqrt{1-p_{\rm em}}|0\rangle_{\rm ph}|1\rangle_{\varepsilon_T}), \\ |0\rangle_T \to |0\rangle_T|0\rangle_{\rm ph}|0\rangle_{\varepsilon_T}. \end{array} \tag{C1}$$

Here the label $_{\rm ph}$ marks the desired photon mode, and ε_T is an environmental mode that marks the erroneously emitted photon. We construct $W_{\rm ph}$ by $W_{\rm ph} = {\rm Tr}_{\varepsilon_T}[M_{\rm ph} \otimes \bar{M}_{\rm ph}]$, in which we trace out the ε_T mode.

The effect of a transmon decay Γ_T similarly leads to a branching of the emission, that $M_{\rm ph} : \mathcal{H}_T \to \mathcal{H}_T \otimes \mathcal{H}_{\rm ph} \otimes \mathcal{H}_{\varepsilon_T}$ becomes

$$M_{\rm ph}: \begin{array}{l} |1\rangle_T \to |0\rangle_T \left(\sqrt{\dfrac{\Gamma_{\rm em}}{\Gamma_{\rm em}+\Gamma_T}}|1\rangle_{\rm ph}|0\rangle_{\varepsilon_T} + \sqrt{\dfrac{\Gamma_T}{\Gamma_{\rm em}+\Gamma_T}}|0\rangle_{\rm ph}|1\rangle_{\varepsilon_T} \right) \\ |0\rangle_T \to |0\rangle_T|0\rangle_{\rm ph}|0\rangle_{\varepsilon_T}. \end{array} \tag{C2}$$

The transmon dephasing leads to an exponential decay of the density matrix elements that are off-diagonal on the transmon basis with rate $\Gamma_\phi/2$. In the regime of $\Gamma_\phi \ll \Gamma_{\rm em}$ the probability accumulates as

$$\int_0^{T_{\rm em}} \frac{\Gamma_\phi}{2}\langle\sigma_{eg}(t)\rangle dt \approx \int_0^\infty \frac{\Gamma_\phi}{2} e^{-\Gamma_{\rm em}t/2} dt = \Gamma_\phi/\Gamma_{\rm em}. \tag{C3}$$

Thus, the mapping will lead to

$$W_{\rm ph}^{10} \to \left(1 - \frac{\Gamma_\phi}{\Gamma_{\rm em}}\right) W_{\rm ph}^{10}, \qquad W_{\rm ph}^{01} \to \left(1 - \frac{\Gamma_\phi}{\Gamma_{\rm em}}\right) W_{\rm ph}^{01}. \tag{C4}$$

in Eq. (B3).

The cavity decay will explicitly depend on the photon emission time $T_{\rm em}$. Since $\Gamma_C \ll \Gamma_{\rm em}$, we can solve the dynamics analytically using the quantum trajectory approach [81] and include up to one jump process of the cavity photon. During the emission process, the decay probability for the Fock state $|n\rangle$ of the cavity mode is approximately $n\Gamma_C T_{\rm em}$. By including a cavity decay environmental mode ε_C, we can write $M_{\rm ph} : \mathcal{H}_C \otimes \mathcal{H}_T \to \mathcal{H}_C \otimes \mathcal{H}_T \otimes \mathcal{H}_{\rm ph} \otimes \mathcal{H}_{\varepsilon_C}$ as

$$M_{\rm ph}: \begin{array}{l} |n\rangle_C|1\rangle_T \to \sqrt{1-n\Gamma_C T_{\rm em}}|n\rangle_C|0\rangle_T|1\rangle_{\rm ph}|0\rangle_{\varepsilon_C} + \sqrt{n\Gamma_C T_{\rm em}}|n-1\rangle_C|0\rangle_T|1\rangle_{\rm ph}|1\rangle_{\varepsilon_C}, \\ |n\rangle_C|0\rangle_T \to \sqrt{1-n\Gamma_C T_{\rm em}}|n\rangle_C|0\rangle_T|0\rangle_{\rm ph}|0\rangle_{\varepsilon_C} + \sqrt{n\Gamma_C T_{\rm em}}|n-1\rangle_C|0\rangle_T|0\rangle_{\rm ph}|1\rangle_{\varepsilon_C}. \end{array} \tag{C5}$$

Similarly, we obtain $W_{\rm ph}$ by $W_{\rm ph} = {\rm Tr}_{\varepsilon_C}[M_{\rm ph} \otimes M_{\rm ph}^\dagger]$. A finite photon emission time also lead to a residue population on $p_{T1}(T_{\rm em}) = e^{-\Gamma_{\rm em}T_{\rm em}} p_{T1}(0)$ on the state $|1\rangle_T$. This can be modeled by a further reduction factor on $p_{\rm em}$ that $p_{\rm em} \to (1 - e^{-\Gamma_{\rm em}T_{\rm em}})p_{\rm em}$.

With the above analysis, we can write down the $M_{\rm ph} : \mathcal{H}_C \otimes \mathcal{H}_T \to \mathcal{H}_C \otimes \mathcal{H}_T \otimes \mathcal{H}_{\rm ph} \otimes \mathcal{H}_{\varepsilon_T} \otimes \mathcal{H}_{\varepsilon_C}$ that includes all the above effects as

$$\begin{aligned} |n\rangle_C|1\rangle_T \to \sqrt{1-n\Gamma_C T_{\rm em}}|n\rangle_C|0\rangle_T \cdot \left(\sqrt{\frac{(1-e^{-\Gamma_{\rm em}T_{\rm em}})\Gamma_{\rm em}p_{\rm em}}{\Gamma_{\rm em}+\Gamma_T}}|1\rangle_{\rm ph}|0\rangle_{\varepsilon_T}|0\rangle_{\varepsilon_C} + \sqrt{1-\frac{(1-e^{-\Gamma_{\rm em}T_{\rm em}})\Gamma_{\rm em}p_{\rm em}}{\Gamma_{\rm em}+\Gamma_T}}|0\rangle_{\rm ph}|1\rangle_{\varepsilon_T}|0\rangle_{\varepsilon_C} \right) \\ + \sqrt{n\Gamma_C T_{\rm em}}|n-1\rangle_C|0\rangle_T \cdot \left(\sqrt{\frac{(1-e^{-\Gamma_{\rm em}T_{\rm em}})\Gamma_{\rm em}p_{\rm em}}{\Gamma_{\rm em}+\Gamma_T}}|1\rangle_{\rm ph}|0\rangle_{\varepsilon_T}|1\rangle_{\varepsilon_C} + \sqrt{1-\frac{(1-e^{-\Gamma_{\rm em}T_{\rm em}})\Gamma_{\rm em}p_{\rm em}}{\Gamma_{\rm em}+\Gamma_T}}|0\rangle_{\rm ph}|1\rangle_{\varepsilon_T}|1\rangle_{\varepsilon_C} \right), \\ |n\rangle_C|0\rangle_T \to \sqrt{1-n\Gamma_C T_{\rm em}}|n\rangle_C|0\rangle_T|0\rangle_{\rm ph}|0\rangle_{\varepsilon_T}|0\rangle_{\varepsilon_C} + \sqrt{n\Gamma_C T_{\rm em}}|n-1\rangle_C|0\rangle_T|0\rangle_{\rm ph}|0\rangle_{\varepsilon_T}|1\rangle_{\varepsilon_C}. \end{aligned} \tag{C6}$$

And further trace out the environmental modes to get $W_{\rm ph} = {\rm Tr}_{\varepsilon_T,\varepsilon_C}[M_{\rm ph} \otimes \bar{M}_{\rm ph}]$. After that, we include the transmon dephasing by applying Eq. (C4), to finish the construction of $W_{\rm ph}$.

Appendix D: Additional scaling data for MPS preparation fidelity

1. Scaling of the error rate χ

As shown in the main text, we can compute the scaling of the coefficient ξ of the exponentially decaying fidelity $\mathcal{F}_{\rm MPS} = e^{-\xi\cdot n}$ with the slope (error rate) ξ as a function of various imperfections. This scaling is numerically shown here in Fig. 9(a-g), where each data point is extracted from a MPDO calculation of the relation between $\mathcal{F}_{\rm MPS}$ and the photon number n (an example is shown in Fig. 3a), with only the specific decoherence channel turned on. For example, in Fig. 9(a) only the transmon decay Γ_T is turned on. From Fig. 9(a-g) we obtain all individual terms in Eq. (12), with non-universal coefficients in Eq. (16) for the cluster state generation with the pulse sequence in Fig. 2. In the regime where the error per photon generation is small, we can estimate the total error ξ by simply adding these individual terms, thus obtaining Eq. (12).

2. Fidelity versus photon number for transmon parameters in Ref. [21]

In Fig. 3(a) we showed the fidelity versus the cluster state photon number for the state-of-the-art experimental parameters shown in section II D. To better compare it with the experimentally demonstrated result [21], here we compute the same relation with the transmon properties reported there, while other parameters stays the same as that in section II D. Specifically, we choose $\Gamma_T = 47.62\,{\rm kHz}$, $\Gamma_\phi = 58.82\,{\rm kHz}$, $\alpha = 2\pi \times -303\,{\rm MHz}$, and $\chi = 2\pi \times -5\,{\rm MHz}$ [21]. The result is shown in Fig. 9(h), from which we get $N_{\rm ph} \approx 47$.

3. Achievable entanglement length $N_{\rm ph}$ with MPS bond dimension D

The entanglement length $N_{\rm ph} = \log 2/\xi$ is determined by the error rate per photon ξ [Eq. (12)].To produce an MPS with bond dimension D, we need to implement unitaries on $2D$-dimensional Hilbert space. As numerical evidence suggesting that [82] the time cost of implementing a general unitary in N-dimensional Hilbert space using the quantum optimal control approach scales as $O(N^2)$, it takes $T^D_{\rm MPS} = O(D^2)$ to implement above unitaries. This lead to increased decoherence as the coefficients $\beta_C, \beta_T, \beta_\phi, \beta_\alpha$ in Eq. (8) are proportional to $T^D_{\rm MPS}$. In the regime of $p_{\rm em} \approx 1$ and $\beta_0 \approx 0$ (typical for current experimental platforms [21, 55]), one can thus estimate the scaling of ξ as

$$\xi \approx T^D_{\rm MPS}\xi_{\rm unit} + \xi^{\rm src}_{\rm em} + \xi^{\rm ph}_{\rm em} \sim O(D^2). \tag{D1}$$

Thus the dominant part lead to a qualitative scaling of $N_{\rm ph} \sim D^{-2}$.

Appendix E: isometric tensor network states

In this section, we provide more details on the definition of isometric tensor network states (isoTNS) [34].

To start, first we recall the definition of the projected entangled pair states (PEPS) [83], which are defined through a network of tensors that are connected with each other, with one tensor at each lattice site (see Fig. 10a). The wavefunction of PEPS is obtained by contracting the connected (virtual) legs of the tensors, as

$$|\Psi_{\rm PEPS}\rangle = \sum_{\{k\}=0}^{d-1} \mathcal{F}_{\rm 2D}(\{B^k_{[i,j]_{lurb}}\})|\{k\}\rangle, \tag{E1}$$

where the $B^k_{[i,j]lurd}$ is a rank-5 tensor on the site (i,j), which has virtual indices $l.u,r,b$ of bond dimension D and physical index k of physical dimension d. And the symbol $\mathcal{F}_{2D}$ denote the contraction of the connected virtual indices. PEPS serve as a natural extension of MPS in higher dimensions, and has wide applications in describing higher-dimensional many body systems [17, 18, 84].

IsoTNS is a subclass of PEPS, where the tensors satisfy certain isometry conditions. The isometry condition means that, when the incoming legs (denoted by the arrows in Fig. 10b) and the physical legs of a tensor are contracted with corresponding legs of the complex conjugate of this tensor, the remaining legs yield an identity. For example, the tensor in the dashed box in Fig. 10(b) obeys

$$\sum_{k,ur} B^k_{[i,j]_{lurb}} \left(B^k_{[i,j]_{l'urb'}}\right)^* = \delta_{bb'}\delta_{ll'}, \tag{E2}$$

which is shown graphically in Fig. 10(c). Moreover, the two red shaded lines in Fig. 10(b) only have incoming arrows, which are termed the *orthogonality hypersurface* of isoTNS, and their intersection is the *orthogonality center* of the isoTNS [34].

As shown in Ref. [1], one can convert an isoTNS tensor $B^k_{[i,j]lurb}$ of the bond dimension D into a 'L'-shaped unitary of the form

$$\hat{B}_{[i,j]} = \sum_{lurb,k} B^k_{[i,j]_{lurb}} |u,k,r\rangle\langle 0,b,l|, \tag{E3}$$

where the indices are identified in Fig. 10(d) for the case of bond dimension $D = d$. Here the rank-5 tensor $B^k_{[i,j]_{lurb}}$ also satisfy the same isometry condition

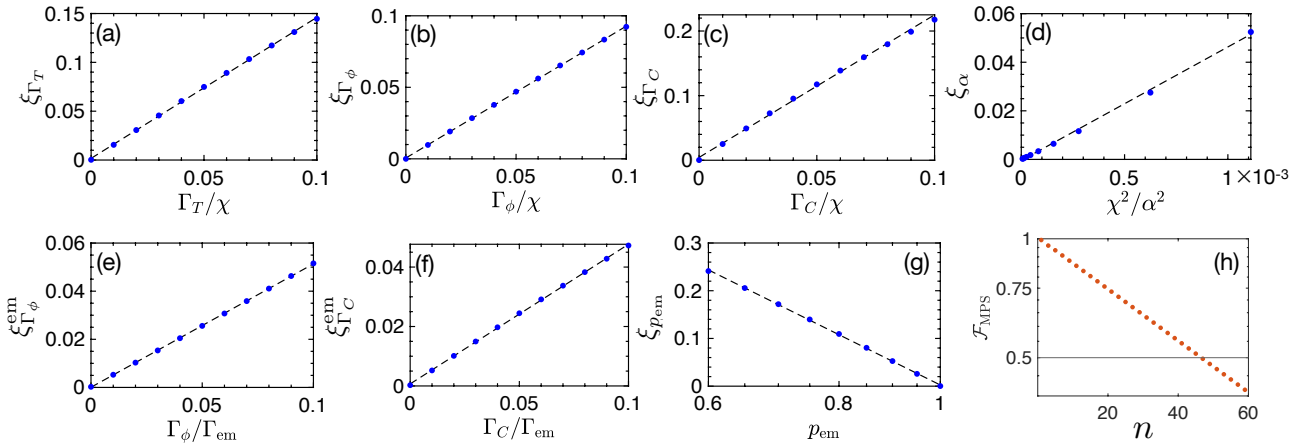

FIG. 9. Scaling of the error rate ξ in $\mathcal{F}_{\rm MPS}$ for creating the cluster state [Eq. (7)] using pulse sequence in Fig. 2 as a function of: the transmon decay during unitary operation (a), transmon dephasing during unitary operation (b), cavity decay during unitary operation (c), transmon anharmonicity during unitary operation (d), transmon dephasing during photon emission (e), cavity decay during photon emission (f), and the photon retrieval efficiency (g). The panel (h) show the MPDO calculation of $\mathcal{F}_{\rm MPS}$ versus the cluster state photon number n, with transmon parameters in Appendix D 2. The horizontal line denotes $\mathcal{F}_{\rm MPS} = 1/2$.

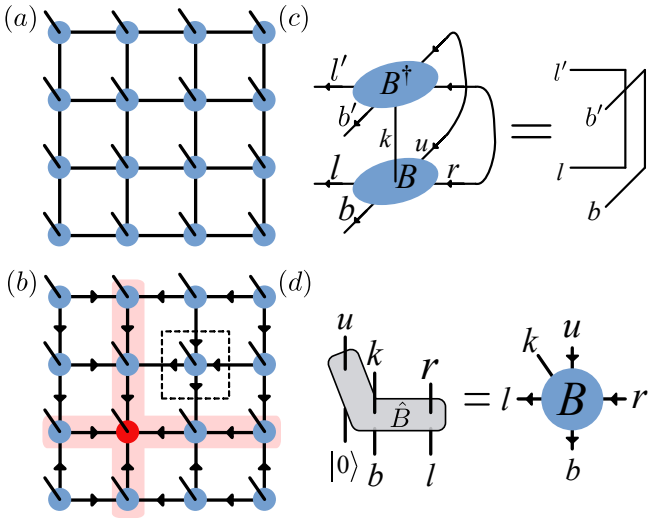

FIG. 10. The projected entangled pair states (PEPS) and isometric tensor network states (isoTNS). (a) PEPS are states represented by a network of tensors, where the tensor at each site is of physical dimension d, and is connected to that of the neighboring sites with virtual bonds of dimension D. (b) IsoTNS are a subclass of PEPS, where the tensors satisfy isometry conditions denoted by the arrows. The red shaded lines denote the *orthogonality hypersurface* of isoTNS, and their crossing point (the red dot) denote the *orthogonality center* of isoTNS. (c) The isometry condition for the tensor inside the dashed box in panel (b). Here the incoming virtual legs and the physical legs of the tensor are contracted with the corresponding legs of the complex conjugate of the tensor, yield identity on the outgoing legs. This is also mathematically shown in Eq. (E2). (d) One can map a three-qubit 'L'-shaped quantum gate (see Fig. 8) to an isoTNS tensor of bond dimension $D = d$.

Eq. (E2). This show that the gates in the photon generation scheme shown in Fig. 8 can be identified as isoTNS tensors. Increasing isoTNS bond dimension corresponds to increasing the arm length of the 'L'-shaped unitary.

In this way, one can generate isoTNS by sequentially applying overlapping 'L'-shape unitaries, which lead to the photonic isoTNS generation protocol discussed in section III C 3. This fact further implies that isoTNS is a subclass of rp-PEPS [1] since we can cover the 'L'-shape unitaries by plaquette unitaries.

1. IsoTNS representation of the toric code

In general, the $\mathbb{Z}_\lambda$ toric code can be written as an isoTNS with the translational-invariant tensor at each site as [37]

$$B^{i_1 i_2 i_3 i_4}_{lurd} = \frac{1}{\lambda}\delta^{i_1}_{l-u}\delta^{i_2}_{u-r}\delta^{i_3}_{r-b}\delta^{i_4}_{b-l}, \tag{E4}$$

where

$$\delta^a_b = \begin{cases} 1, & a = b \mod \lambda \\ 0, & \text{otherwise.} \end{cases} \tag{E5}$$

This is a tensor of bond dimension λ and physical dimension λ^4, and satisfies the isometry condition Eq. (E2).

Appendix F: Control universality of $H_{\rm array}(t)$

Here we show the Hamiltonian $H_{\rm array}(t)$ [Eq. (19)] can universally control the Hilbert space $\mathcal{H}^{L_C\times m}_{\rm array} = (\mathcal{H}_{\rm src})^{\otimes L_C\times m}$. Let us consider case of two cQED sequential photon sources coupled to each other ($L_C = 1$ and

$m = 2$), that the whole Hilbert space is

$$\mathcal{H}_{\text{array}}^{1\times 2} = \mathcal{H}_T \otimes \mathcal{H}_C \otimes \mathcal{H}_C \otimes \mathcal{H}_T. \tag{F1}$$

We know the Hamiltonian for each sequential photon source can control one $\mathcal{H}_{\text{src}}$ universally. This means one can create arbitrary Hamiltonians that act on each Hilbert space $\mathcal{H}_C$ of the cavity mode (see Eq. (F2) below). Together with the bilinear interaction H_{int}^{ij} [Eq. (18)] between two cavities, one can apply an analogous argument in Ref. [85], that by arithmetic operation and taking commutators between the bilinear coupling H_{int}^{12} [c.f. Eq. (18)] and single cavity Hamiltonians

$$H_1 = \text{poly}(a_1, a_1^\dagger), \quad H_2 = \text{poly}(a_2, a_2^\dagger), \tag{F2}$$

we can generate arbitrary polynomial form of Hamiltonian

$$H_{12} = \text{poly}(a_1, a_1^\dagger, a_2, a_2^\dagger) \in \mathcal{H}_C \otimes \mathcal{H}_C. \tag{F3}$$

This immediately implies that we can universally control the Hilbert space of two cavities [85]. Together with universal control on each sequential photon source, we can use Lemma 5.5 of Ref. [86] to combine the universality of two $\mathcal{H}_{\text{src}}$ and $\mathcal{H}_C \otimes \mathcal{H}_C$ to the whole $\mathcal{H}_{\text{array}}^{1\times 2}$, which shows that we can universally control $\mathcal{H}_{\text{array}}^{1\times 2}$ with $H_{\text{array}}(t)$ (here $L_C = 1$ and $m = 2$). By repeatedly applying Lemma 5.5 of Ref. [86], one can show $H_{\text{array}}(t)$ is further able to control $\mathcal{H}_{\text{array}}^{L_C\times m}$.

[1] Z.-Y. Wei, D. Malz, and J. I. Cirac, "Sequential generation of projected entangled-pair states," arXiv:2107.05873 [quant-ph].
[2] J. L. O'Brien, A. Furusawa, and J. Vučković, Nature Photonics **3**, 687 (2009).
[3] N. Gisin and R. Thew, Nature photonics **1**, 165 (2007).
[4] H. J. Kimble, Nature **453**, 1023 (2008).
[5] C. L. Degen, F. Reinhard, and P. Cappellaro, Reviews of Modern Physics **89**, 1 (2017).
[6] D. C. Burnham and D. L. Weinberg, Physical Review Letters **25**, 84 (1970).
[7] H. S. Zhong, Y. Li, W. Li, L. C. Peng, Z. E. Su, Y. Hu, Y. M. He, X. Ding, W. Zhang, H. Li, L. Zhang, Z. Wang, L. You, X. L. Wang, X. Jiang, L. Li, Y. A. Chen, N. L. Liu, C. Y. Lu, and J. W. Pan, Physical Review Letters **121**, 1 (2018).
[8] K. M. Gheri, C. Saavedra, P. Törmä, J. I. Cirac, and P. Zoller, Physical Review A **58**, R2627 (1998).
[9] C. Saavedra, K. M. Gheri, P. Törmä, J. I. Cirac, and P. Zoller, Physical Review A **61**, 62311 (2000).
[10] C. Schön, E. Solano, F. Verstraete, J. I. Cirac, and M. M. Wolf, Physical Review Letters **95**, 1 (2005).
[11] C. Schön, K. Hammerer, M. M. Wolf, J. I. Cirac, and E. Solano, Physical Review A **75**, 1 (2007).
[12] N. H. Lindner and T. Rudolph, Physical Review Letters **103**, 1 (2009).
[13] K. Tiurev, M. H. Appel, P. L. Mirambell, M. B. Lauritzen, A. Tiranov, P. Lodahl, and A. S. Sørensen, arXiv:2007.09295.
[14] Z.-Y. Wei, D. Malz, A. González-Tudela, and J. I. Cirac, Phys. Rev. Research **3**, 23021 (2021).
[15] D. Perez-Garcia, F. Verstraete, M. M. Wolf, and J. I. Cirac, arXiv:0608197 [quant-ph].
[16] U. Schollwöck, Annals of Physics **326**, 96 (2011).
[17] R. Orús, Annals of Physics **349**, 117 (2014).
[18] J. I. Cirac, D. Perez-Garcia, N. Schuch, and F. Verstraete, "Matrix product states and projected entangled pair states: Concepts, symmetries, and theorems," (2020), arXiv:2011.12127.
[19] I. Schwartz, D. Cogan, E. R. Schmidgall, Y. Don, L. Gantz, O. Kenneth, N. H. Lindner, and D. Gershoni, Science **354**, 434 (2016).
[20] C. Eichler, J. Mlynek, J. Butscher, P. Kurpiers, K. Hammerer, T. J. Osborne, and A. Wallraff, Physical Review X **5**, 1 (2015).
[21] J.-C. Besse, K. Reuer, M. C. Collodo, A. Wulff, L. Wernli, A. Copetudo, D. Malz, P. Magnard, A. Akin, M. Gabureac, G. J. Norris, J. I. Cirac, A. Wallraff, and C. Eichler, Nature Communications **11**, 1 (2020).
[22] S. E. Economou, N. Lindner, and T. Rudolph, Physical Review Letters **105**, 1 (2010).
[23] M. Gimeno-Segovia, T. Rudolph, and S. E. Economou, Physical Review Letters **123**, 70501 (2019).
[24] A. Russo, E. Barnes, and S. E. Economou, New Journal of Physics **21**, 55002 (2019).
[25] R. Bekenstein, I. Pikovski, H. Pichler, E. Shahmoon, S. F. Yelin, and M. D. Lukin, Nature Physics **16**, 676 (2020).
[26] S. Bartolucci, P. Birchall, H. Bombin, H. Cable, C. Dawson, M. Gimeno-Segovia, E. Johnston, K. Kieling, N. Nickerson, M. Pant, F. Pastawski, T. Rudolph, and C. Sparrow, arXiv:2101.09310.
[27] H. Pichler, S. Choi, P. Zoller, and M. D. Lukin, Proceedings of the National Academy of Sciences **114**, 11362 (2017).
[28] I. Dhand, M. Engelkemeier, L. Sansoni, S. Barkhofen, C. Silberhorn, and M. B. Plenio, Physical Review Letters **120** (2018).
[29] S. Xu and S. Fan, APL Photonics **3** (2018), 10.1063/1.5044248.
[30] K. Wan, S. Choi, I. H. Kim, N. Shutty, and P. Hayden, "Fault-tolerant qubit from a constant number of components," arXiv:2011.08213.
[31] Y. Zhan and S. Sun, Physical Review Letters **125**, 223601 (2020).
[32] Y. Shi and E. Waks, arXiv:2101.07772.
[33] H. Bombin, I. H. Kim, D. Litinski, N. Nickerson, M. Pant, F. Pastawski, S. Roberts, and T. Rudolph, arXiv:2103.08612.
[34] M. P. Zaletel and F. Pollmann, Physical Review Letters **124**, 37201 (2020).

[35] M. Hein, J. Eisert, and H. J. Briegel, Physical Review A **69**, 62311 (2004).
[36] F. Verstraete, M. M. Wolf, D. Perez-Garcia, and J. I. Cirac, Physical Review Letters **96**, 1 (2006).
[37] N. Schuch, I. Cirac, and D. Pérez-García, Annals of Physics **325**, 2153 (2010).
[38] M. A. Levin and X. G. Wen, Physical Review B **71**, 1 (2005).
[39] Z.-C. Gu, M. Levin, B. Swingle, and X.-G. Wen, Physical Review B **79**, 85118 (2009).
[40] O. Buerschaper, M. Aguado, and G. Vidal, Physical Review B **79**, 085119 (2009).
[41] T. Soejima, K. Siva, N. Bultinck, S. Chatterjee, F. Pollmann, and M. P. Zaletel, Physical Review B **101**, 1 (2020).
[42] Note that the string-net states are originally defined on the hexagonal lattice [38]. Since one can embed a hexagonal lattice into a square lattice, one can create string-net states using the schemes we show in this paper, which are based on square lattices.
[43] Y. Takeuchi, T. Morimae, and M. Hayashi, Scientific Reports **9**, 1 (2019).
[44] W. Asavanant, Y. Shiozawa, S. Yokoyama, B. Charoensombutamon, H. Emura, R. N. Alexander, S. Takeda, J. I. Yoshikawa, N. C. Menicucci, H. Yonezawa, and A. Furusawa, Science (New York, N.Y.) **366**, 373 (2019).
[45] K. J. Satzinger, Y. Liu, A. Smith, C. Knapp, M. Newman, C. Jones, Z. Chen, C. Quintana, X. Mi, A. Dunsworth, and Others, arXiv:2104.01180.
[46] G. Semeghini, H. Levine, A. Keesling, S. Ebadi, T. T. Wang, D. Bluvstein, R. Verresen, H. Pichler, M. Kalinowski, R. Samajdar, and Others, .
[47] M. Jarzyna and R. Demkowicz-Dobrzański, Physical Review Letters **110**, 1 (2013).
[48] B. Koczor, S. Endo, T. Jones, Y. Matsuzaki, and S. C. Benjamin, New Journal of Physics **22** (2020), 10.1088/1367-2630/ab965e.
[49] K. Chabuda, J. Dziarmaga, T. J. Osborne, and R. Demkowicz-Dobrzański, Nature Communications **11**, 1 (2020).
[50] K. Azuma, K. Tamaki, and H. K. Lo, Nature Communications **6** (2015), 10.1038/ncomms7787.
[51] M. Reagor, W. Pfaff, C. Axline, R. W. Heeres, N. Ofek, K. Sliwa, E. Holland, C. Wang, J. Blumoff, K. Chou, M. J. Hatridge, L. Frunzio, M. H. Devoret, L. Jiang, and R. J. Schoelkopf, Physical Review B **94**, 1 (2016).
[52] F. W. Strauch, Physical Review Letters **109**, 1 (2012).
[53] S. Machnes, E. Assémat, D. Tannor, and F. K. Wilhelm, Physical Review Letters **120** (2018).
[54] H. J. Briegel and R. Raussendorf, Physical Review Letters **86**, 910 (2001).
[55] R. W. Heeres, P. Reinhold, N. Ofek, L. Frunzio, L. Jiang, M. H. Devoret, and R. J. Schoelkopf, Nature Communications **8** (2017).
[56] K. S. Chou, J. Z. Blumoff, C. S. Wang, P. C. Reinhold, C. J. Axline, Y. Y. Gao, L. Frunzio, M. H. Devoret, L. Jiang, and R. J. Schoelkopf, Nature **561**, 368 (2018).
[57] J. Lee, C. Arenz, H. Rabitz, and B. Russell, New Journal of Physics **20** (2018), 10.1088/1367-2630/aac6f3.
[58] Y. Huang, (), arXiv:1505.00772.
[59] A. M. Dalzell and F. G. Brandão, Quantum **3** (2019), 10.22331/q-2019-09-23-187.
[60] Y. Huang, (), arXiv:1903.10048.
[61] N. Schuch and F. Verstraete, arXiv:1711.06559.
[62] B. Pirvu, G. Vidal, F. Verstraete, and L. Tagliacozzo, Physical Review B **86**, 75117 (2012).
[63] Here we do not include the transmons in the ancilla space due to their relatively short coherence time compared to the photons in the cavities. However, in principle, one can include the transmons into the ancilla as well to further increase its Hilbert space dimension.
[64] C. Wang, Y. Y. Gao, P. Reinhold, R. W. Heeres, N. Ofek, K. Chou, C. Axline, M. Reagor, J. Blumoff, K. M. Sliwa, L. Frunzio, S. M. Girvin, L. Jiang, M. Mirrahimi, M. H. Devoret, and R. J. Schoelkopf, Science **352**, 1087 (2016).
[65] Y. Y. Gao, B. J. Lester, Y. Zhang, C. Wang, S. Rosenblum, L. Frunzio, L. Jiang, S. M. Girvin, and R. J. Schoelkopf, Physical Review X **8**, 21073 (2018).
[66] The source point of rp-PEPS is exactly defined as the location of the first plaquette unitary.
[67] W. Huggins, P. Patil, B. Mitchell, K. Birgitta Whaley, and E. Miles Stoudenmire, Quantum Science and Technology **4** (2019), 10.1088/2058-9565/aaea94.
[68] J.-G. Liu, Y.-H. Zhang, Y. Wan, and L. Wang, Physical Review Research **1**, 1 (2019).
[69] S. Rosenblum, Y. Y. Gao, P. Reinhold, C. Wang, C. J. Axline, L. Frunzio, S. M. Girvin, L. Jiang, M. Mirrahimi, M. H. Devoret, and R. J. Schoelkopf, Nature Communications **9** (2018), 10.1038/s41467-018-03059-5.
[70] E. Dennis, A. Kitaev, A. Landahl, and J. Preskill, Journal of Mathematical Physics **43**, 4452 (2002).
[71] A. Y. Kitaev, Annals of Physics **303**, 2 (2003).
[72] Y. Liu, A. Smith, K. Shtengel, and F. Pollmann, In preparation.
[73] S. S. Bullock and G. K. Brennen, Journal of Physics A: Mathematical and Theoretical **40**, 3481 (2007).
[74] G. Duclos-Cianci and D. Poulin, Physical Review A **87**, 1 (2013).
[75] F. H. E. Watson, H. Anwar, and D. E. Browne, Physical Review A **92**, 1 (2015).
[76] N. Ofek, A. Petrenko, R. Heeres, P. Reinhold, Z. Leghtas, B. Vlastakis, Y. Liu, L. Frunzio, S. M. Girvin, L. Jiang, M. Mirrahimi, M. H. Devoret, and R. J. Schoelkopf, Nature **536**, 441 (2016).
[77] P. Campagne-Ibarcq, A. Eickbusch, S. Touzard, E. Zalys-Geller, N. E. Frattini, V. V. Sivak, P. Reinhold, S. Puri, S. Shankar, R. J. Schoelkopf, L. Frunzio, M. Mirrahimi, and M. H. Devoret, Nature **584**, 368 (2020).
[78] W.-L. Ma, M. Zhang, Y. Wong, K. Noh, S. Rosenblum, P. Reinhold, R. J. Schoelkopf, and L. Jiang, Physical Review Letters **125**, 110503 (2019).
[79] T. Schulte-Herbrüggen, A. Spörl, N. Khaneja, and S. J. Glaser, Journal of Physics B: Atomic, Molecular and Optical Physics **44** (2011).
[80] M. Abdelhafez, D. I. Schuster, and J. Koch, Physical Review A **99**, 52327 (2019).
[81] M. B. Plenio and P. L. Knight, Reviews of Modern Physics **70**, 101 (1998).
[82] J. Lee, C. Arenz, H. Rabitz, and B. Russell, New Journal of Physics **20**, 1 (2018).
[83] F. Verstraete and J. I. Cirac, arXiv:0407066 [cond-mat].
[84] R. Orús, Nature Reviews Physics **1**, 538 (2019).
[85] S. Lloyd and S. L. Braunstein, Physical Review Letters **82**, 1784 (1999).
[86] T. Hofmann and M. Keyl, arXiv:1712.07613.